

Supplementary information

- S1. Electrochemical Measurements
 - Table S1: Position of SWV peak and overpotential
 - Figure S1: CV and SWV of ionic liquid-modified FePC/G
- S2. Advantages, disadvantages, and errors of oxygen permeability measurements
- S3. Choice of time for the Shoup-Szabo fitting
 - Figure S2: Results of Shoup-Szabo fitting as a function of fitting time
- S4. Results of oxygen transport measurements
 - Figure S3: Results of gravimetric and volumetric oxygen solubility measurements
 - Figure S4: CV and Shoup-Szabo fitting for electrochemical oxygen transport measurements
 - Figure S5: Results of diffusion coefficient fitting, using Fick's law
- S5. Literature data on oxygen permeability in ionic liquids
 - Figure S6: Comparison of literature data on oxygen solubility in selected ionic liquids
- S6. Estimating the resistance to mass transport across the interface
 - Figure S7: Example of chronoamperometry experiment with increasing layer thickness
 - Figure S8: Steady-state oxygen reduction current, as a function of the layer thickness
- S7. Derivation of oxygen transport equations
- S8. Thermal analysis of ionic liquid-modified catalysts
 - Figure S9: DSC of ionic liquid-modified FePC/G
 - Figure S10: TG-MS results of ionic liquid-modified FePC/G and mass assignments
- S9. Porosimetry analysis of ionic liquid-modified catalysts
 - Figure S11: N₂-sorption isotherm of pristine catalyst and BET surface area as a function of ionic liquid loading
 - Figure S12: N₂-sorption isotherm and pore size distribution, for different ionic liquid loading
- S10. X-ray adsorption spectra
 - Figure S13: XAS spectra
- S11. Characterization of pristine FePC/G catalyst
 - Figure S14: N₂ sorption and porosimetry results
 - Figure S15: XPS results
 - Table S2: XPS survey results
 - Table S3: XPS nitrogen peak fitting results
 - Figure S16: SEM image of the pristine catalyst
- S12. Bibliography

S1. Electrochemical Measurements

Figure S1c shows the raw square-wave voltammetry data for FePC/G modified by the addition of ionic liquids. Data were collected in N_2 -saturated 0.1M KOH, using a potential step of 4mV, modulation amplitude of 20mV and a frequency of 2Hz, resulting in a scan-rate of 8mVs⁻¹. Figure S1d was obtained by subtracting the capacitive background and only shows the high potential peak.

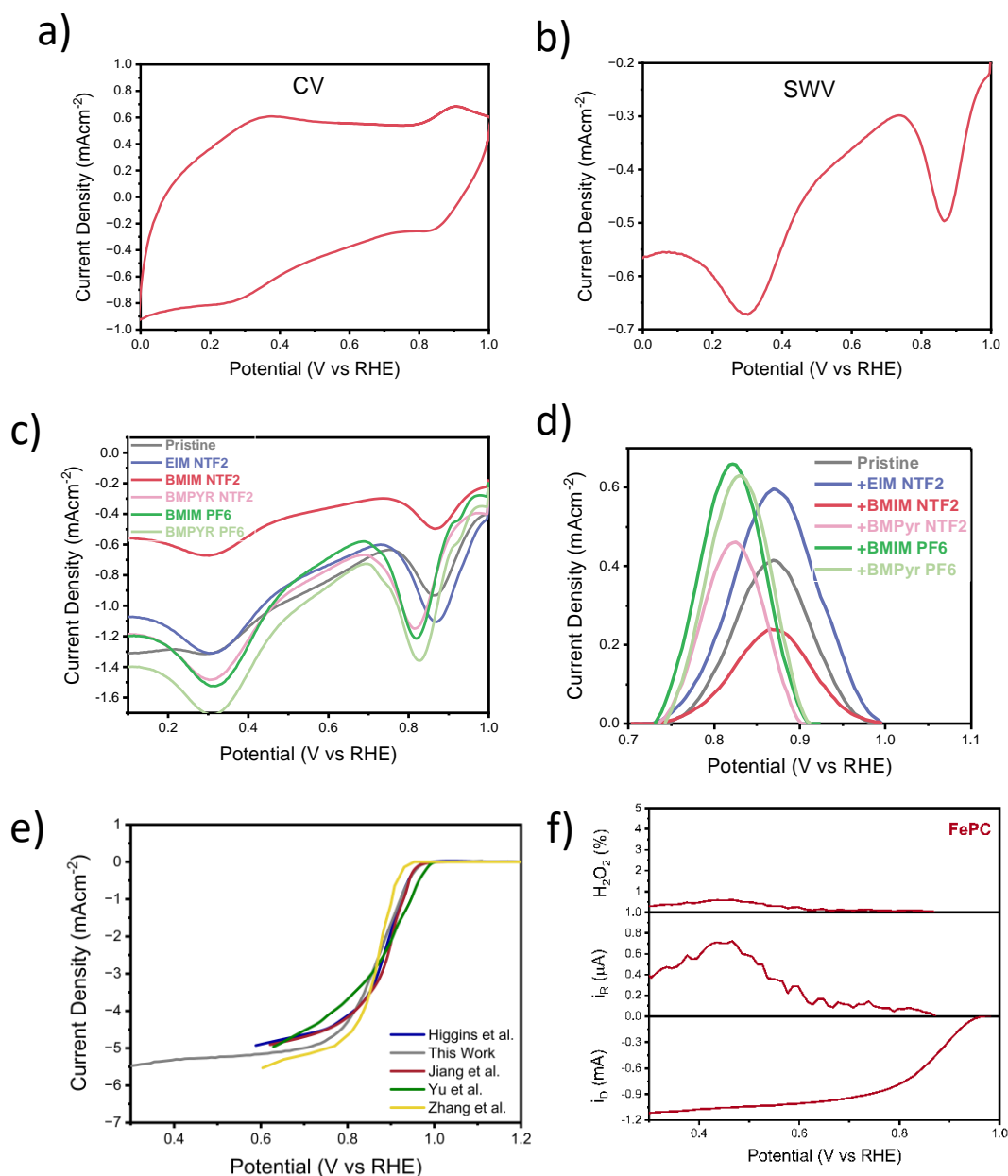


Figure S1: a) and b) show the CV and SWV respectively of FePC with BMIM NTF₂, to show the increased resolution offered by SWV. Both were obtained in N_2 -saturated 0.1M KOH in static condition, the CV was measured at a scan rate of 50 mV/s, while the SWV was obtained using a potential step of 4mV, modulation amplitude of 20mV and a frequency of 2Hz

c) Cathodic square wave voltammogram scans of FePC/G modified by the addition of ionic liquids. Obtained in N_2 -saturated 0.1M KOH, using a potential step of 4mV, modulation amplitude of 20mV and a frequency of 2Hz, resulting in a scan-rate of 8mVs⁻¹ d) zoom-in on the background-subtracted high potential SWV peak

e) Comparison of pristine catalyst (FePC deposited on graphene) oxygen reduction activity, with literature reported data. Literature data are from Higgins et al.¹ (in blue), Jiang et al.² (in red), Yu et al.³ (in green), Zhang et al.⁴ (in yellow).

f) RRDE results for the pristine catalyst FePC/G. From top to bottom, the graph shows the peroxide production efficiency, the current measured at the ring and the current measured at the disc, as a function of the applied potential. Data were obtained in O₂-saturated 0.1M KOH at a rotational speed of 400 rpm, and 10mV/s scan rate

S2. Advantages, disadvantages and source of error of the main techniques used to determine gas solubility and diffusivity in ionic liquids

In this manuscript, we offer a comparison of oxygen transport parameters obtained with the three most common methods: gravimetric, volumetric and electrochemical.

The gravimetric method is based on monitoring the weight of an ionic liquid sample, as the system is pressurized with oxygen gas, while the volumetric method has a similar working principle, based on monitoring the pressure of the system after the introduction of a known volume of oxygen. Finally, for the electrochemical technique, the measurement of oxygen transport data relies on the one-electron reduction of oxygen on a platinum micro-electrode, conducted in an in-house built T-cell.

One of the main advantages of the gravimetric technique is the possibility of monitoring the sample weight during the degas stage, which ensures complete degassing and is not present for the other techniques. Additionally, gravimetric analysis can go to higher pressure than atmospheric, which ensures a higher oxygen sorption and hence lower error. This is also theoretically possible for the other methods, but practically inaccessible with the set-up utilized. For the case of volumetric methods, it is possible to obtain pressure-dependent data, but only up to 1 bar, while for electrochemical ones, only the solubility at 1bar oxygen pressure is attainable. On the other hand, the accuracy of gravimetric measurements relies on an accurate buoyancy correction, particularly considering the low solubility of oxygen in ionic liquids. These were obtained by performing blank experiments and correcting the results but introduced uncertainty regarding the oxygen density as a function of pressure and the density of the ionic liquid.

Regarding the volumetric method, it should be noted that an accurate determination of solubility depends on the precise determination of the free volume, i.e. the volume of the sample holder, not occupied by the sample. This is obtained by introducing a known volume of argon and monitoring the pressure, under the assumption that argon absorption in the ionic liquid is negligible. In addition, the accuracy of the measurements depends on the magnitude of the absorbed volume, compared to the free volume.

Regarding the determination of diffusivity coefficients, both gravimetric and volumetric techniques, rely on fitting the time-dependent data to the solution of Fick's second law, as shown in the equation below.

$$\bar{C}_{O_2} = \frac{1}{L} \int_0^L C_{O_2} dt$$

$$\bar{C}_{O_2} = C_{O_2,s} \left(1 - 2 \left(1 - \frac{C_{O_2,o}}{C_{O_2,s}} \right) \sum_{\lambda=0}^{\infty} \exp\left(\frac{\lambda_n D t}{L^2}\right) / \lambda_n \right), \quad \lambda_n = \left(n + \frac{1}{2}\right)^2 \pi^2$$

(1)

Where \bar{C} is the average concentration of oxygen in the sample, C_0 and C_s are the initial and steady-state concentration respectively and L is the sample thickness. Figure shows a typical gravimetric experiment, where the time-dependent oxygen concentration (in purple) has been fitted with Fick's second law (in red). In this case, we believe that the main origin on uncertainty relies on the sample thickness, which is calculated starting from the mass of the ionic liquid, its density, and the geometry of the container.

Finally, electrochemical methods have the main advantage of being relatively simple and time-effective, while requiring a very limited amount of ionic liquid (down to 10 μ L). As previously mentioned, this technique relies on the assumption that the one-electron reduction of oxygen is the only reaction in the system, which excludes the presence of residual water or impurities. This is particularly critical when considering that in-line monitoring of the degassing status or temperature control are impossible with the set-ups so far reported, leaving the degas process to rely on vacuum at room temperature for an arbitrary amount of time. It should be noticed that, if water remained in the system, it would lead to an under-estimation of the average number of electrons transferred (n) and an over-estimation of oxygen solubility. Additionally, while other techniques obtain solubility data from steady-state values, the electrochemical method calculates oxygen solubility (C_{O_2}) and diffusivity (D_{O_2}) simultaneously, by fitting the time-dependent data to either the Cottrel or the Shoup-Szabo equation. Since Compton and co-workers have shown the superiority of Shoup and Szabo equation in modelling chronoamperometry experiments with microelectrodes, this model, shown in equation (2), has been used throughout this work.⁵

$$I = -4nFD_{O_2}C_{O_2}r_d f(\tau), \quad \tau = \frac{4D_{O_2}t}{r_d^2}$$

$$f(\tau) = 0.7854 + 0.88863\tau^{-\frac{1}{2}} + 0.2146e^{-0.7823\tau^{-\frac{1}{2}}}$$
(2)

Where F is the faraday constant and r_d is the radius of the microelectrode.

A note on permeability: oxygen permeability in this manuscript is defined as the product of oxygen solubility and diffusivity, divided by the oxygen partial pressure. This value is proportional to the oxygen flux. It is similar to the concept of gas permeability used in membranes, and uses the same units of barrer.

For example, if oxygen solubility is 10mM and the diffusivity is $12 * 10^{-6} \frac{cm^2}{s}$ at 1 bar oxygen partial pressure, the permeability would be calculated as follows:

$$Permeability_{O_2} = \frac{S_{O_2}D_{O_2}}{P_{O_2}} = 10mM * 12 * 10^{-6} \frac{cm^2}{s} * \frac{1}{1bar} = 1.2 * 10^{-10} \frac{mol}{cm s bar}$$

$$= 358 \text{ barrer}$$

Where S_{O_2} is the solubility, D_{O_2} is the diffusion coefficient and P_{O_2} is the oxygen partial pressure

S3. Choice of time for the Shoup-Szabo fitting

The Shoup-Szabo equation was used to fit the time-dependent chronoamperometry data and obtain an estimation of the oxygen solubility and diffusivity in ionic liquids. However, the results obtained

depend on the choice of fitting time, which therefore needs to be selected carefully. The first 20ms are discarded, to minimize current contributions from non-Faradaic charging, but this equation remains sensitive to the total fitting time. Xiong et al. have analysed the optimum fitting time for the determination of the concentration and diffusion coefficient of ferrocene and they found the optimum to be between 0.15s and 0.5s.⁶ However, a higher value is expected for ionic liquids, due to their greater viscosity. To select an appropriate fitting time, this equation was fitted using times of 0.2s to 20s, to identify a range over which the obtained solubility and diffusivity values are independent of the chosen time. As it can be observed in **Figure S2**, this seems to be the case for fitting times of 0.2s to 2s, above which the values start to diverge. However, it should be also noticed that the product of solubility and diffusivity ($C \cdot D$, in green in **Figure S2**), appears independent on the fitting time, suggesting that this might be a more reliable metric to export from such experiments. For this work, 1s was selected as a fitting time. This choice is further supported by the fact that the diffusion coefficients obtained with 1s fitting time are in line with those obtained with the gravimetric and volumetric techniques.

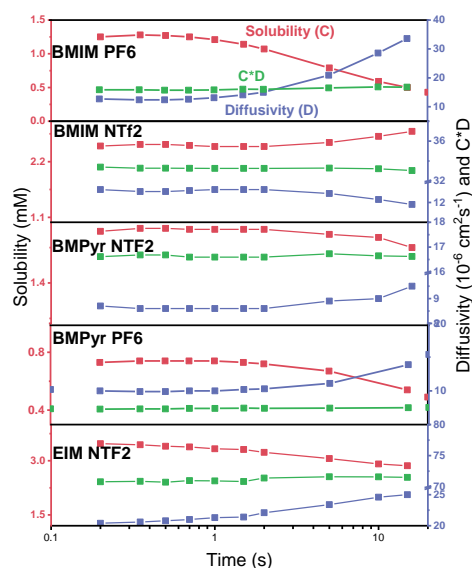


Figure S2: Results of the Shoup-Szabo fitting, as a function of the fitting time. As it can be observed, the oxygen solubility (in red) and diffusivity (in purple) in the ionic liquids varies with the fitting time, while the product of the two (in green) remains constant.

S4 Results of the oxygen solubility and diffusivity measurement in ionic liquids

The results of oxygen solubility as a function of pressure, determined with gravimetric and volumetric methods are shown in figure S3, while figure S4 shows an example of the Fick's second law fitting, used to determine the diffusion coefficient with the same techniques. Finally, Figure S5 shows an example of the results of the Shoup-Szabo fitting, used to determine oxygen solubility and diffusivity with the chronoamperometry electrochemical method.

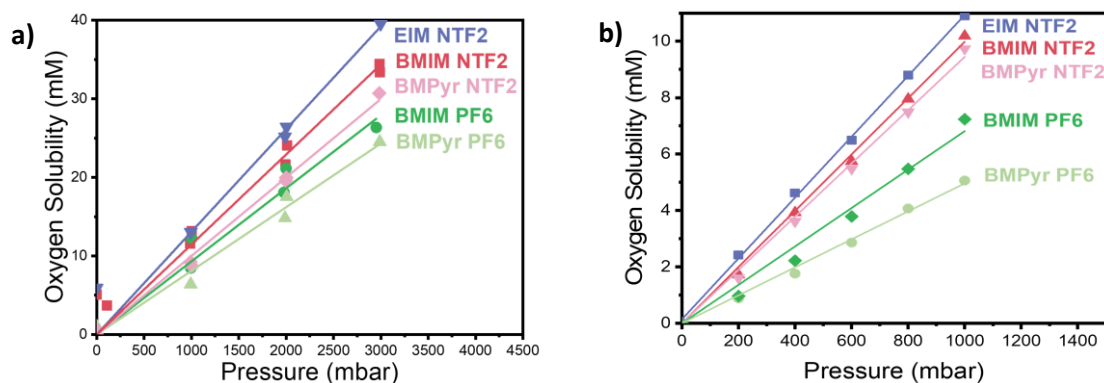


Figure S3: Oxygen solubility as a function of the oxygen pressure, in selected ionic liquids. Determined with a gravimetric (a) and volumetric (b) method

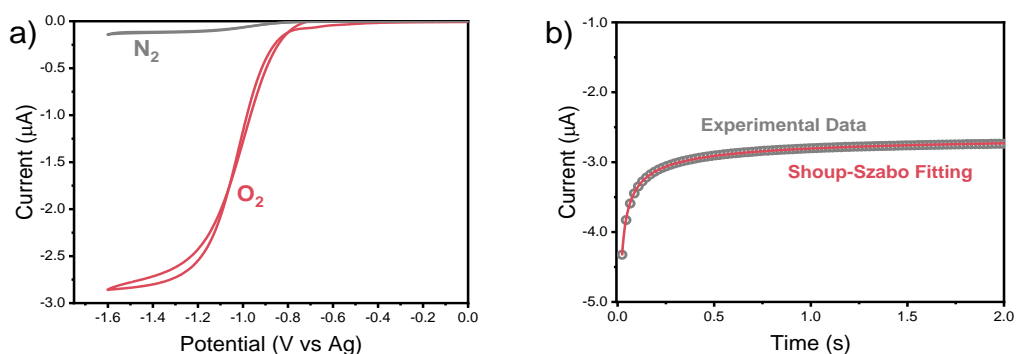


Figure S5: a) Cyclic voltammogram of an ionic liquid (BMIM PF6) saturated with nitrogen (in grey) and oxygen (in red). Data obtained in a T-cell with a silver wire pseudo-reference electrode
b) Experimental chronoamperometry data for a potential step from 0V vs Ag to -1.6V vs Ag (in grey). Data obtained in a T-cell with a silver wire pseudo-reference electrode and oxygen saturated BMIM PF6 electrolyte. In red is shown the fitting obtained with the Shoup-Szabo equation

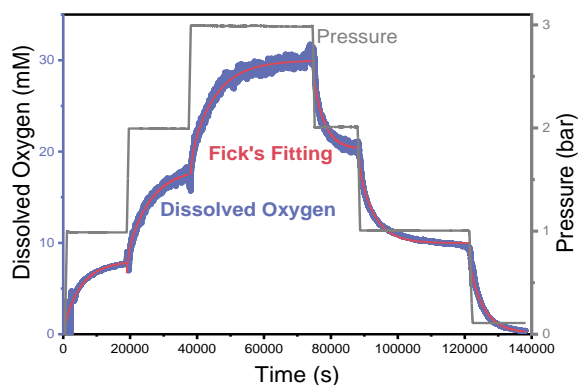


Figure S4: In purple is the experimental value for the amount of oxygen dissolved in the ionic liquid (BMIM PF6) as a function of time. In red is the fitting obtained by applying the solution to Fick's second law. The applied oxygen pressure is shown in grey.

S5. Literature data on oxygen permeability in ionic liquids

Figure S6a shows the oxygen solubility results reported in literature and determined in this work, for a selection of ionic liquids. As it can be observed, a wide range of results have been reported, which highlights the necessity of conducting a systematic study using different experimental techniques, to ensure the reliability and reproducibility of the results. For example, for the case of BMPyr NTF₂, the reported oxygen solubility seems to fall in two groups, one reporting 8 to 10 mM and another one with values around 2 to 4 mM. The results obtained in this work with gravimetric and volumetric techniques (9.7mM) fall in the first group, while the results obtained with the electrochemical method falls in the second (1.9mM). While the low oxygen solubility and high experimental error can partially explain the discrepancy of reported results, we propose that the existence of these two distinct groups results from the fact that the first two methods calculate oxygen solubility, while the last one determines oxygen activity.

Figure S6b shows the solubility and diffusivity of oxygen in selected ionic liquid, modified by the extension of the fluorinated chain. While solubility increases with the degree of fluorination, this also increases viscosity, with a detrimental effect on diffusivity. This goes to show that there is a trade-off between solubility and diffusivity, and that the two cannot be independently increased.

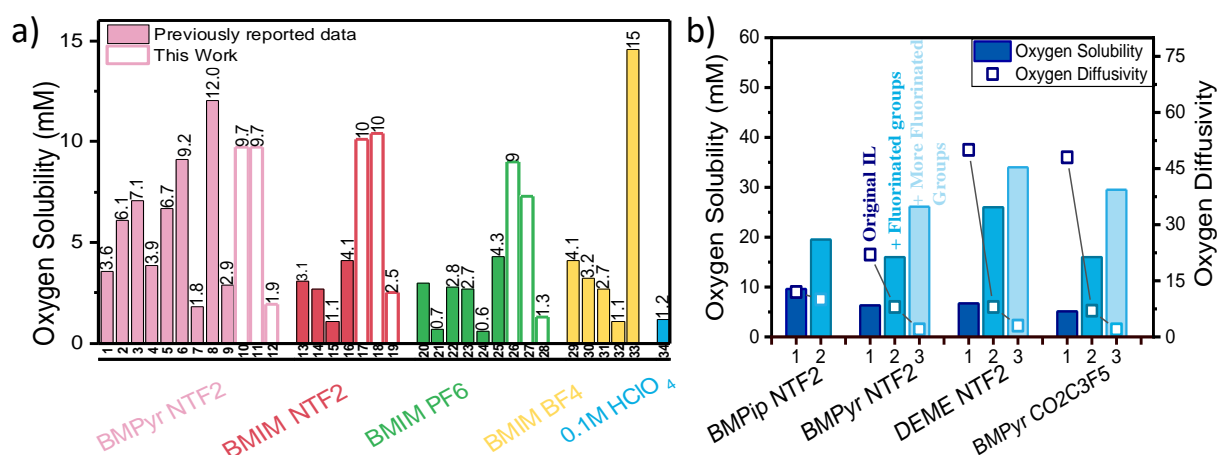


Figure S6: a) Comparison of oxygen solubility data in selected ionic liquids reported in literature. The values have been previously reported as follows: 1) Huang et al.⁷, 2) Evans et al.⁸, 3) Xiao et al.⁹, 4) Nakamoto et al.¹⁰, 5) Vanhouette et al.¹¹, 6) Neale et al.¹², 7) Anthony et al.¹³, 8) Song et al.¹⁴, 9) Monaco et al.¹⁵, 10-12) this work, 13) Huang et al.⁷, 14) Xiao et al.⁹, 15) Anthony et al.¹³, 16) Bahadur et al.¹⁶, 17-19) this work, 20) Huang et al.⁷, 21) Anthony et al.¹³, 22) Afzal et al.¹⁷, 23) Kumean et al.¹⁸, 24) Anthony et al.¹⁹, 25) Jacquemin et al.²⁰, 26-28) this work, 29) Huang et al.⁷, 30) Afzal et al.¹⁷, 31) Jacquemin et al.²⁰, 32) Zhang et al.²¹, 33) Husson-Borg et al.²² Modified with permission Favero et al.²³ Copyright © 2020 The Authors. Advanced Energy and Sustainability Research published by Wiley-VCH GmbH
b) Oxygen solubility (columns) and diffusivity (squares) of fluorinated ILs. In blue are shown the original IL, whereas data in lighter blue represent increased fluorination of the original ILs. Presented data were originally reported by Vanhouette et al.¹¹. Reproduced with permission from Favero et al.²³ Copyright © 2020 The Authors. Advanced Energy and Sustainability Research published by Wiley-VCH GmbH

S6. Estimating the resistance to mass transport across the interface

Throughout this project, it has been assumed that oxygen transport across the interface is fast and therefore that $1/k_i$ is negligible. To confirm this hypothesis, we have performed chronoamperometry experiments in a variation of the T-cell. Once again, silver wires are used as pseudo-reference and counter electrode and a collar positioned on top of the working electrode allows to test less than a ml of electrolyte. The main difference between this cell and the one previously introduced, is the use of a Pt working electrode, rather than a micro-electrode. As a result, compared to the T-cell, where oxygen was transported by convergent diffusion, in this configuration oxygen transport is linear and can be therefore described with the Fick's diffusion described above. For the case of calculating oxygen transport in ionic liquids, convergent diffusion is preferred, because a reliable fitting can be obtained from 100 long experiments (while linear diffusion can take hours to equilibrate) and because it does not require any knowledge of the ionic liquid thickness, eliminating a possible source of inaccuracy. However, to observe the mass transfer across the electrolyte/ionic liquid interface, we need linear diffusion and therefore we use this second configuration.

First of all, different thicknesses of the electrolyte were tested. Consequently, a second layer of ionic liquid was added. In both cases, the potential was stepped from the OCV to a value

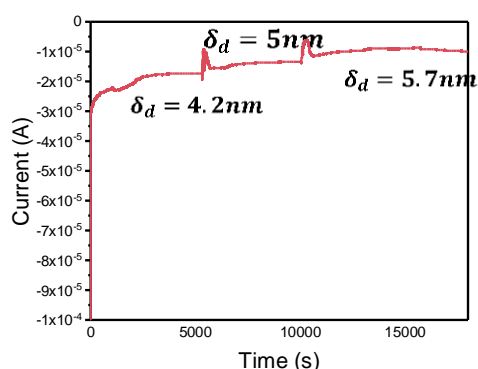


Figure S 7: Example of a chronoamperometry step experiment, where the thickness of the electrolyte has been gradually increased

when oxygen reduction is diffusion-limited and the current was recorded in a chronoamperometry experiment. Figure S6 shows a typical chronoamperometry curve, where the thickness of the ionic liquid layer has been gradually increased. The thickness of the aqueous and IL electrolytes was determined by weighting the electrode.

Figure S7 shows the reciprocal of the steady state current, as a function of the thickness of the electrolyte layers. Initially, only the aqueous electrolyte was used and from the slope of the fitted (see **Figure S8a**), one can obtain a constant which depends on the oxygen transport and geometry of the system ($k_e = S_e D_e n_e F A$).

$$\frac{1}{i} = \frac{\delta_e}{S_e D_e n_e F A} = \frac{\delta_e}{k_e}$$

Consequently, a thin layer of electrolyte is deposited on top of the ionic liquid and the experiment is repeated while varying the thickness of this electrolyte layer. In this case, the steady state current is determined by the diffusion in the two layers and by the resistance to mass transfer across the interface (k_i). In **Figure S8** Figure S b, a 3mm aqueous electrolyte was used and the thickness of the ionic liquid was varied. Finally, in **Figure S8c**, the thickness of

both layered were varied. The difference between the reciprocal of the measured current and the electrolyte contribution to the total current ($\frac{1}{i} - \frac{1}{i_e} = \frac{1}{i} - \frac{1}{k_e \delta_e}$) as been plotted as a function of ionic liquid thickness. In this way, the resulting line is proportional to k_{IL}^{-1} and intercepts the y axis at k_i^{-1} .

$$\frac{1}{i} = \frac{\delta_{IL}}{S_{IL} D_{IL} n_e F A} + \frac{1}{k_i} + \frac{\delta_e}{S D_e n_e F A} \rightarrow \frac{1}{i} - \frac{\delta_e}{k_e} = \frac{\delta_{IL}}{k_{IL}} + \frac{1}{k_i}$$

The intercepts in Figure 11c is $-0.0001 \mu A^{-1}$, indicating that the resistance to oxygen transport across the interface is negligible and within experimental error.

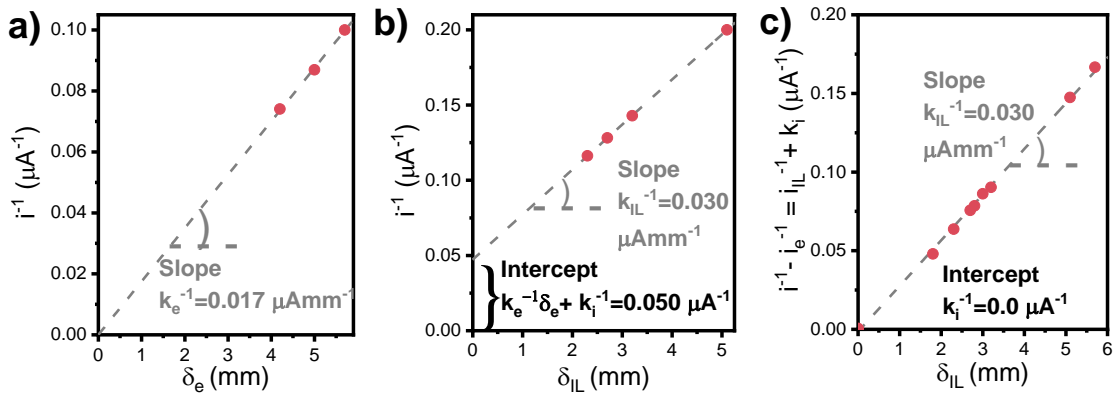


Figure S 8: Steady-state oxygen reduction current, in the diffusion limited region. This value was obtained by stepping the potential to a value where the reaction is diffusion limited and waiting for the current to stabilize. The experiments were performed in the T-cell shown in figure 6, with a Pt macroelectrode and a cap containing layers of 0.1M KOH and ionic liquids (shown here is BMPyr NTf₂).

- a) Results obtained in the pure aqueous electrolyte (0.1M KOH). The slope is proportional to the mass transfer coefficient of oxygen in the aqueous electrolyte.
- b) Results obtained with a 3mm electrolyte layer and various thicknesses of the ionic liquid. The slope is proportional to the mass transfer coefficient of oxygen in the ionic liquid and the intercept represents the constant contribution of the aqueous electrolyte to oxygen transport, which is in agreement with the value determined in Figure a) for a thickness of 3mm
- c) Results obtained by varying the thickness of both the ionic liquid and aqueous electrolyte layers. Here, the contribution of the aqueous electrolyte is removed from the total current ($i^{-1} - i_e^{-1}$), so that the plotted current is only due to oxygen transport in the ionic liquid (k_{IL}^{-1} =slope) and to the resistance to oxygen transport across the interface (k_i^{-1} =intercept)

S7. Derivation of equations for the transport of oxygen from the bulk of the electrolyte to the surface of catalyst modified with a layer of ionic liquid, in RDE configuration

Approximation of diffusion-limited current

A first approximation to determine the diffusion-limited current is based on the simple Levich equation. In the diffusion-limited region of the linear sweep voltammogram, the oxygen reduction rate is equal to the transport of oxygen to the catalyst surface, which is controlled by Fick's diffusion

$$J = -D_e \frac{\partial C}{\partial x} = -\frac{D_e}{\delta_D} S_e$$

Where J is the oxygen flux, and D, C and S are the diffusion coefficient, concentration and thermodynamics activity of oxygen at equilibrium with 1bar oxygen partial pressure

(solubility*activity coefficient) respectively. The thickness of the diffusion layer depends on the rotational speed (ω) of the electrode and on the viscosity of the electrolyte (ν), as shown in the following equation:

$$\delta_D = 1.61 D_{O_2,e}^{\frac{1}{3}} \nu^{\frac{1}{6}} \omega^{-\frac{1}{2}}$$

By combining the above equations with the Faraday law, one can obtain the well-known Levich equation, which predicts that the diffusion-limited current is proportional to the oxygen solubility in the electrolyte and the diffusion coefficient to the power of 2/3.

$$i_D = 0.62 n_e F D_{O_2}^{\frac{2}{3}} \nu^{-\frac{1}{6}} \omega^{\frac{1}{2}} S_{O_2} \rightarrow i_D \propto D_{O_2}^{\frac{2}{3}} S_{O_2}$$

However, since the diffusion layer (≈ 10 to $20 \mu\text{m}$) is much thicker than the ionic liquid, the majority of this space is occupied by the electrolyte and hence the diffusion thickness is relatively independent on the properties of the ionic liquid.

For all the calculations in the manuscript, an electron transfer number of 4 is assumed. As it can be seen in Figure S1f, the peroxide production for the pristine FePC/G sample is potential dependent but is below 1% over the whole potential range investigated. All the ionic liquid-modified samples showed similar behaviour, with a peroxide production lower than 1% in the potential range of 0.3-1 V vs RHE. Therefore, for simplicity, an electron transfer number of 4 was used for all the samples.

More accurate description of oxygen flux in diffusion-limited conditions – derivation of equation (3) in the article

A more realistic depiction of the oxygen concentration profile is shown in Figure 4a and Figure 4b in the main article. In absence of the ionic liquid, oxygen concentration is zero at the catalyst surface and equal to oxygen solubility in the electrolyte at a distance equal to the diffusion thickness. When we add a thin film of ionic liquid on the surface of the catalyst, oxygen is still fully depleted at the catalyst surface and oxygen transport is still determined by diffusion, but there is a discontinuity in oxygen concentration at the ionic liquid/electrolyte interface. Assuming that the resistance to oxygen transfer across the interface is negligible and hence that this equilibrium is instantaneously established, oxygen flux (J_{O_2}), which in diffusion-limited conditions is equal to the rate of reaction of oxygen (r_{O_2}) can be calculated as shown in equation, based on Fick's law of diffusion

$$r_{O_2} = J_{O_2,e} = \frac{D_e}{\delta_D} (S_e - a_{e,i}) = J_{O_2,IL} = \frac{D_{IL}}{\delta_{IL}} (a_{IL,i} - 0)$$

Where δ_D, δ_{IL} are the diffusion thickness and the thickness of the ionic liquid layer, D_e and D_{IL} are the diffusion coefficients of oxygen in the electrolyte and ionic liquid $S_{O_2,e}$ is the thermodynamics activity of oxygen at equilibrium with 1bar oxygen partial pressure (solubility*activity coefficient) in the electrolyte. $a_{e,i}$ and $a_{IL,i}$ are the thermodynamics activity of oxygen at the interface, on the electrolyte and ionic liquid sides respectively. Knowing that the $a_{e,i}$ and $a_{IL,i}$ relate to the solubility ratio (SR) as follows, the unknown $a_{e,i}$ and $a_{IL,i}$ can be removed and one can obtain the oxygen flux.

$$\frac{a_{IL,i}}{a_{e,i}} = SR = \frac{S_{IL}}{S_e}$$

$$a_{IL,i} = C_{e,i} SR$$

$$\frac{D_e S_e}{\delta_D - \delta_{IL}} - \frac{D_e a_{e,i}}{\delta_D - \delta_{IL}} = \frac{D_{IL}}{\delta_{IL}} a_{e,i} SR$$

Isolating $C_{e,i}$

$$C_{e,i} = \frac{\frac{D_e S_e}{\delta_D - \delta_{IL}}}{\frac{D_e}{\delta_D - \delta_{IL}} + \frac{D_{IL} SR}{\delta_{IL}}} = \frac{D_e S_e \delta_{IL}}{D_e \delta_{IL} + D_{IL} SR (\delta_D - \delta_{IL})}$$

Substituting this expression in the original equation we obtain

$$r_{O_2} = J_{O_2} = \left(\frac{\delta_D - \delta_{IL}}{D_e} + \frac{\delta_{IL}}{D_{IL} SR} \right)^{-1} S_e$$

To compare these theoretical predictions to the experimental results, it is necessary to obtain an estimate for the thickness of the ionic liquid layer. This value is enclosed between the “geometric thickness” ($\delta_{D,Geom} = V_{IL} A_{Geom}^{-1} = 350-450\text{nm}$, **Figure 3d**) and the “BET thickness” ($\delta_{D,BET} = V_{IL} A_{BET}^{-1} = 6-8\text{nm}$, **Figure 3c**) depending on the structure and porosity of the support, on the loading of the ionic liquid and on its distribution in the pores. A thickness of 100nm was used for all the ionic liquids, as it offered good agreement with experimental data.

Oxygen flux in mixed kinetics and diffusion conditions – derivation of equation (4) in the article

When both the oxygen transport and reaction kinetics play a role, the oxygen concentration at the catalyst surface is no more null and the oxygen flux can be described by equation 3

$$J_{O_2,e} = \frac{D_e}{\delta_D - \delta_{IL}} (S_e - a_{e,i}) = J_{O_2,IL} = \frac{D_{IL}}{\delta_{IL}} (a_{IL,i} - a_0) = r_{O_2} = k_{rx} a_0$$

Where r_{O_2} is the rate of consumption of oxygen, k_{rx} is the oxygen reaction constant (which is potential dependent) and a_0 is the concentration of oxygen at the catalyst's surface. Again knowing that $a_{IL,i} = SR * a_{e,i}$ we have 3 unknowns ($a_{e,i}$, $a_{IL,i}$ and a_0) and 3 equations.

Starting from

$$J_{O_2,e} = \frac{D_e}{\delta_D - \delta_{IL}} (S_e - a_{e,i}) = J_{O_2,IL} = \frac{D_{IL}}{\delta_{IL}} (a_{IL,i} - a_0)$$

we can isolate C_0

$$\frac{D_e}{\delta_D - \delta_{IL}} (S_e - a_{e,i}) = \frac{D_{IL}}{\delta_{IL}} (a_{e,i} SR - a_0)$$

$$a_0 = a_{e,i} SR + \frac{D_e \delta_{IL}}{(\delta_D - \delta_{IL}) D_{IL}} (S_e - a_{e,i})$$

We can similarly isolate an expression from the equation below, and using the fact that $a_{IL,i} = SR C_{e,i}$ for a_0

$$J_{O_2,IL} = \frac{D_{IL}}{\delta_{IL}} (a_{IL,i} - a_0) = r_{O_2} = k_{rx} a_0$$

$$a_0 = \frac{\frac{D_{IL} SR a_{e,i}}{\delta_{IL}}}{k_{rx} + \frac{D_{IL}}{\delta_{IL}}} = \frac{D_{IL} SR a_{e,i}}{k_{rx} \delta_{IL} + D_{IL}}$$

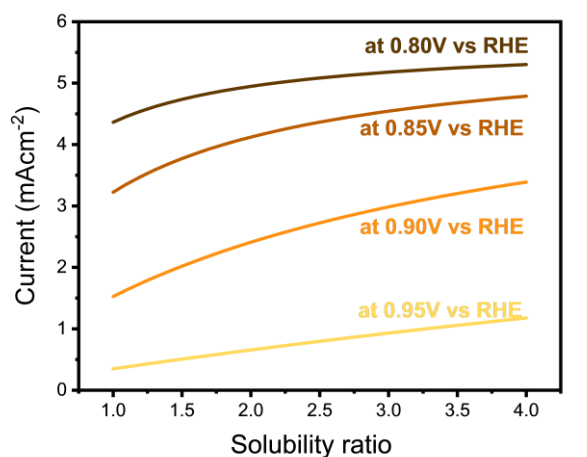
Combining the two expressions obtained for C_o , we can isolate an expression for $C_{e,i}$

$$\begin{aligned} a_0 &= a_{e,i} SR + \frac{D_e \delta_{IL}}{(\delta_D - \delta_{IL}) D_{IL}} (S_e - a_{e,i}) = \frac{SR a_{e,i}}{\frac{k_{rx} \delta_{IL}}{D_{IL}} + 1} \\ a_{e,i} &= \frac{D_e \delta_{IL} S_e}{(\delta_D - \delta_{IL}) D_{IL}} \frac{1}{\frac{D_{IL} SR}{k_{rx} \delta_{IL} + D_{IL}} - SR + \frac{D_e \delta_{IL}}{(\delta_D - \delta_{IL}) D_{IL}}} \\ &= \frac{D_e \delta_{IL} S_e}{(\delta_D - \delta_{IL}) D_{IL}} \frac{k_{rx} \delta_{IL} + D_{IL}}{k_{rx} \delta_{IL} SR + \frac{D_e \delta_{IL}^2 k_{rx}}{(\delta_D - \delta_{IL}) D_{IL}} + \frac{D_e \delta_{IL}}{(\delta_D - \delta_{IL})}} \\ &= \frac{D_e \delta_{IL} S_e}{(\delta_D - \delta_{IL}) D_{IL}} \frac{(k_{rx} \delta_{IL} + D_{IL})(\delta_D - \delta_{IL}) D_{IL}}{k_{rx} \delta_{IL} SR (\delta_D - \delta_{IL}) D_{IL} + D_e \delta_{IL}^2 k_{rx} + D_e \delta_{IL} D_{IL}} = \\ &= \frac{S_e (k_{rx} \delta_{IL} + D_{IL}) D_e}{k_{rx} SR (\delta_D - \delta_{IL}) D_{IL} + k_{rx} D_e \delta_{IL} + D_e D_{IL}} = \end{aligned}$$

Substituting this expression in $J_{O_2,e} = \frac{D_e}{\delta_D - \delta_{IL}} (S_e - C_{e,i})$ and rearranging we obtain

$$\begin{aligned} J_{O_2,e} &= \frac{D_e}{\delta_D - \delta_{IL}} S_e \left(1 - \frac{(k_{rx} \delta_{IL} + D_{IL}) D_e}{k_{rx} SR (\delta_D - \delta_{IL}) D_{IL} + k_{rx} D_e \delta_{IL} + D_e D_{IL}} \right) = \\ &= \frac{D_e}{\delta_D - \delta_{IL}} S_e \left(\frac{k_{rx} SR (\delta_D - \delta_{IL}) D_{IL} + k_{rx} D_e \delta_{IL} + D_e - (k_{rx} \delta_{IL} + D_{IL}) D_e}{k_{rx} SR (\delta_D - \delta_{IL}) D_{IL} + k_{rx} D_e \delta_{IL} + D_e D_{IL}} \right) \\ &= \frac{D_e S_e}{\delta_D - \delta_{IL}} \left(\frac{k_{rx} SR (\delta_D - \delta_{IL}) D_{IL}}{k_{rx} SR (\delta_D - \delta_{IL}) D_{IL} + k_{rx} D_e \delta_{IL} + D_e D_{IL}} \right) = \\ \rightarrow J_{O_2} = r_{O_2} &= \frac{k_{rx} SR D_{IL} D_e S_e}{k_{rx} SR (\delta_D - \delta_{IL}) D_{IL} + k_{rx} D_e \delta_{IL} + D_e D_{IL}} \end{aligned}$$

The reaction constant could be further related to the potential via the Butler-Volmer equation for highly irreversible reactions $k = k_0 \exp\left(\frac{azF}{RT} \eta\right)$



(of oxygen in the ionic liquid, when adding a 1nm monolayer)

Figure S9: Oxygen reduction current as a function of oxygen solubility ratio in the ionic liquid compared to the electrolyte. Results are shown for a monolayer of ionic liquid (estimated as 1 nm thickness), for different applied potential. These predictions are determined from the above analysis, where oxygen flux is converted to a current, by multiplying it by the average number of electrons (4 from RRDE results) and the Faraday constant.

S8. Thermal analysis of ionic liquid modified catalysts

The samples were thoroughly degassed under vacuum for 12h at 80°C before the analysis, to remove the influence of absorbed water on the physicochemical properties of the ionic liquid. Figure S9 shows the DSC thermograms of bulk EIm NTF₂, pristine catalyst and catalyst with 40%w and 80%w ionic liquid. The pristine catalyst features an exothermic peak at around 200°C, attributable to the reduction of graphene oxide in the support,²⁴ and a very broad endothermic decomposition peak. The bulk ionic liquid features two crystallization peaks, at -58°C and -37°C and two melting peaks at 0°C and -10°C.²⁵ A glass transition can be observed at -89°C and, finally, the ionic liquid undergoes an exothermic decomposition starting at 390°C.

This has been observed, among others, by Singh and co-workers, who reported that confinement of BMIM BF₄ in a SiO₂ matrix causes a shift in both the crystallization and melting temperature, while the impregnation of this ionic liquid on MCM-41 causes the disappearance of both features.²⁶

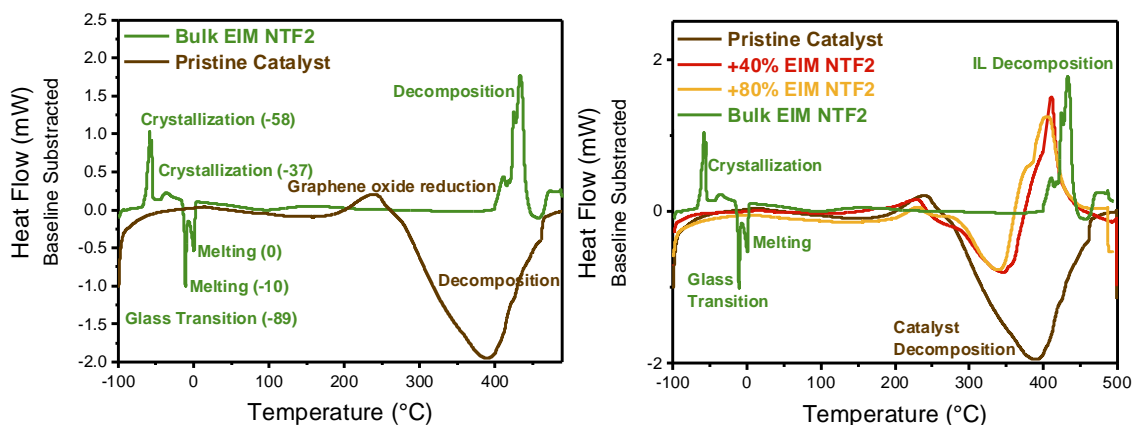


Figure S9: Differential scanning calorimetry heating curves of the bulk ionic liquid (in green), the pristine catalyst (in brown) and the catalyst with ionic liquid layer (yellow and red). Positive heat flow are considered exothermic.

Figure S10a shows the TG-MS results, and Figure S10b summarizes the assigned species. As it can be observed, the pristine catalyst rapidly degrades above 350°C releasing characteristic carbon, nitrogen and oxygen-

containing compounds, such as carbon monoxide ($m/z=28$), carbon dioxide ($m/z=44$) and ammonia ($m/z=17$). At 1000°C about 3% of the initial weight is retained, attributed to iron.

On the other side, the bulk ionic liquid starts to decompose at 222°C , with the release of fluorinated and sulfonated compounds originated from the decomposition of the anion, such as F ($m/z=19$), CF_3 ($m/z=69$), SO ($m/z=48$), SO_2 ($m/z=64$).

Figure S10c compares the release of fluorine and sulphur dioxide, as determined by TG-MS, for the bulk and confined ionic liquid. It clearly shows that ionic liquid-specific decomposition products are released at lower temperature in the confined ionic liquid. The same figure compares 80%w EIm NTF₂ and 190%w EIm NTF₂ deposited on the catalyst. It can be observed that with higher ionic liquid loading, the decomposition signal increases, along with the onset temperature, which shifts closer to that of the bulk liquid. This thermal stability drop has been previously observed by Singh et al, for a similar ionic liquid (EMIM BF₄) confined in a MCM-41 matrix.²⁵ They proposed that the CH imidazolium ring might interact with oxygen on the support surface, causing a premature decomposition of the cation. Additionally, they similarly observed that the onset decomposition of confined ionic liquids approaches the bulk temperature, as the loading increases. This shows that the ionic liquid interacts with the support, but also that higher loadings result in higher proportion of bulk-like ionic liquid.

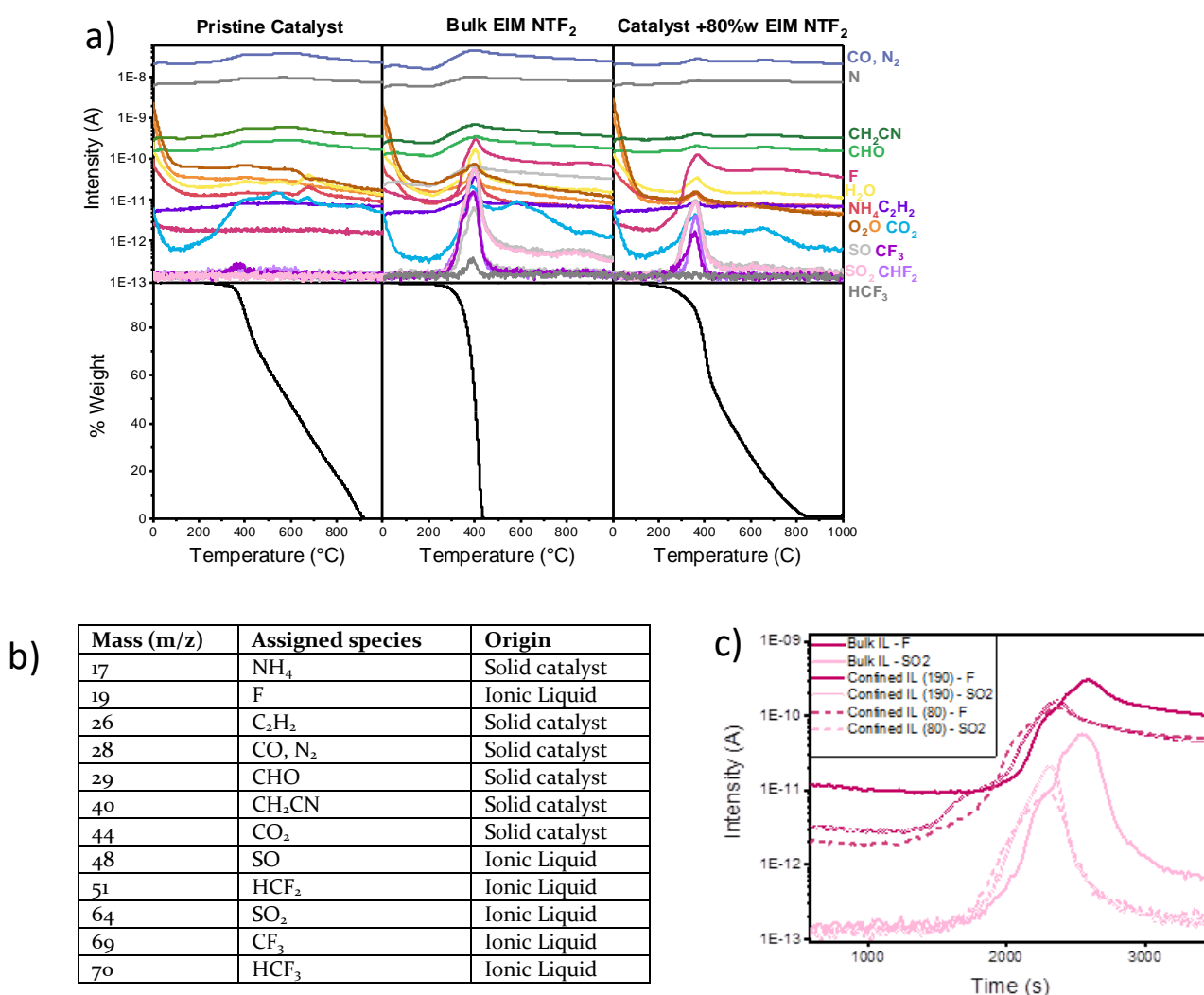


Figure S10: a) Mass spectrometry (top) and thermal gravimetric measurements of, from left to right, the pristine catalyst, the bulk ionic liquid and the catalyst with a layer of EIM NTF₂. To make the mass spectrometry data ore readable, only selected masses are shown

b) Mass assignment

c) Mass spectrometry intensity signal for F (dark pink) and SO_2 (light pink), for the bulk ionic liquid EIM NTF₂ (solid line) and confined ionic liquid, i.e. the catalyst with the addition of 190% EIM NTF₂ (double line) and 80% EIM NTF₂ (dashed line).

S9. Porosimetry analysis of ionic liquid-modified catalysts

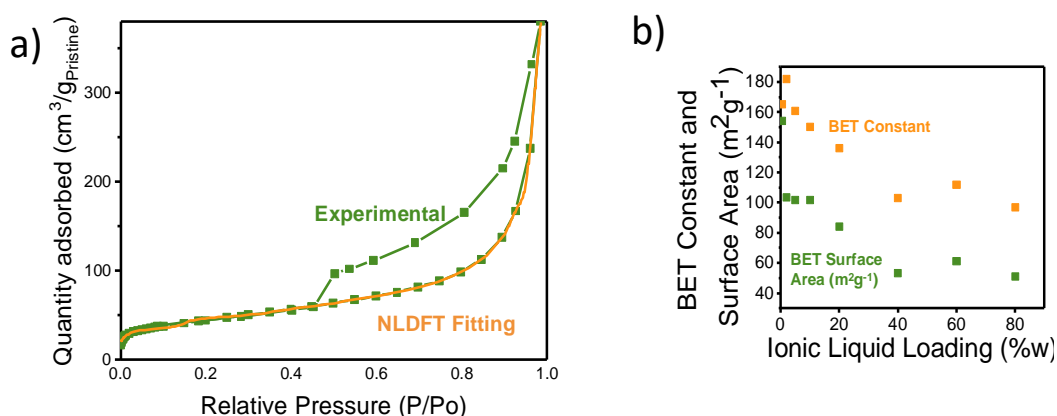


Figure S11: a) N₂ sorption isotherm of the pristine FePC/G catalyst. Comparison of the experimental data (green) and the fitting with NLDFT for carbon slit pores b) Surface area calculated by BET (normalized to the mass of the pristine catalyst), as a function of the loading of the ionic liquid EIM NTf₂

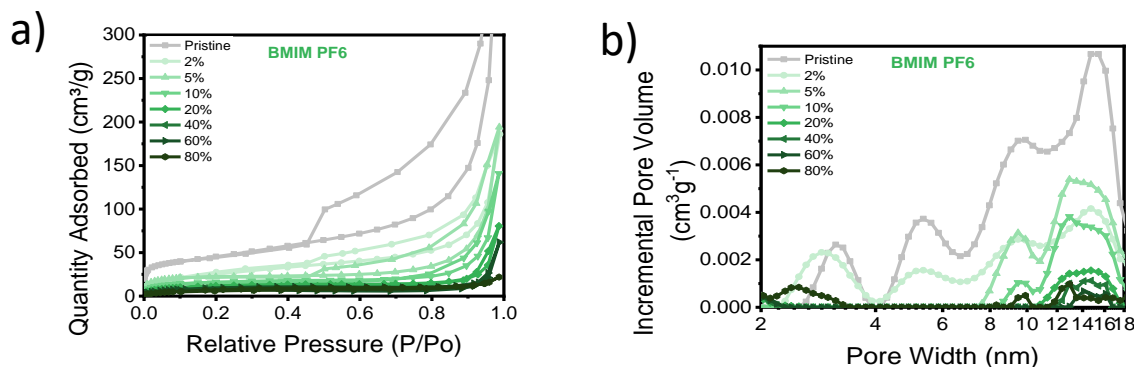


Figure S12: a) N₂-sorption isotherm and b) pore diameter distribution, normalized to the mass of the pristine catalyst. From grey to dark green, the curves represent the FePC/G catalyst, modified with an incrementally increasing amount of the ionic liquid BMIm PF₆

Porosimetry analysis was used to gain a thorough understanding of the ionic liquid distribution in the catalyst pores. **Figure S11** shows the N₂ sorption isotherm of the pristine FePC/G catalyst. According to IUPAC classification, the pristine catalyst shows a typical IV N₂ isotherm, with a typical H₁ hysteresis caused by the presence of micropores.²⁷ The original catalyst presents a BET surface area of 157 m²g⁻¹ and a broad pore diameter distribution, with maxima around 3, 5 and 10 nm. The micropore volume is 0.005 cm³g⁻¹ while the total pore volume is 0.55 cm³g⁻¹. The pore size distribution was determined using NLDFT, which provided a good fitting, as shown in figure S10a.

The ionic liquid decreases the surface area measured by N₂ sorption. The surface area decreases rapidly with the initial liquid addition but stabilizes around 50 m²g⁻¹. Several factors could be causing the overestimation of the BET surface area:

- One possible explanation behind the fact that the surface area does not decrease after 40%w loading is the surface and bulk adsorption by the ionic liquid itself. However, this is about two orders of magnitude lower than the calculated surface area and therefore this alone cannot explain the value observed.²⁸
- Another thing to take into consideration is that the accuracy of the measurement decreases with lower N₂ sorption. However, the surface area determined at 40%w is about a third of the initial value, therefore the error is not expected to be increased significantly.

- Finally, as more ionic liquid covers the surface of the catalyst, the interaction of nitrogen with the surface can be significantly altered. Heinze et al. have previously observed that ionic liquid deposited on a silica support, cause a strong shift in the BET constant, a parameter that represents the affinity of the surface with the adsorbate.²⁸ **Figure S1b** shows that a similar phenomenon occurs here. The pristine catalyst features a BET constant of 183, which is in the typical range for porous materials. The impregnation with ionic liquids causes this constant to drop to about 100, indicating the weakening of the adsorbate-surface interaction. This could cause a minor overestimation of the BET surface area calculated at high IL loading but would still not explain a value as high as 50 m²g⁻¹.

S10. XAS of ionic liquid-modified catalyst

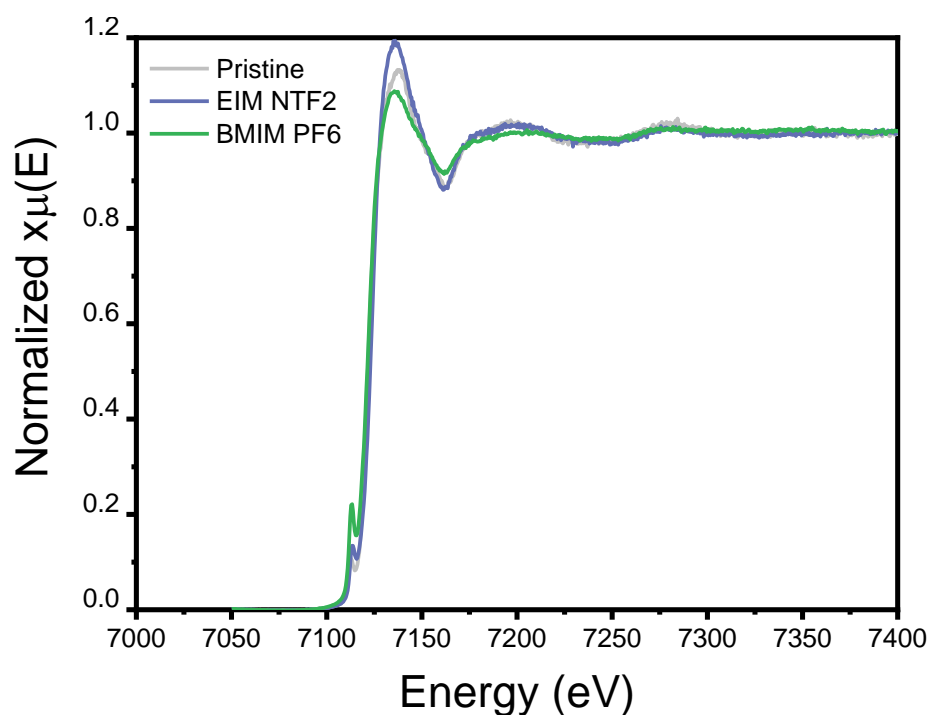


Figure S13: EXAFS of the FePC catalyst, modified by the addition of 20% EIM NTF2 (purple) and BMIM PF6 (green).

S11. Characterization of the pristine catalyst

Porosimetry analysis

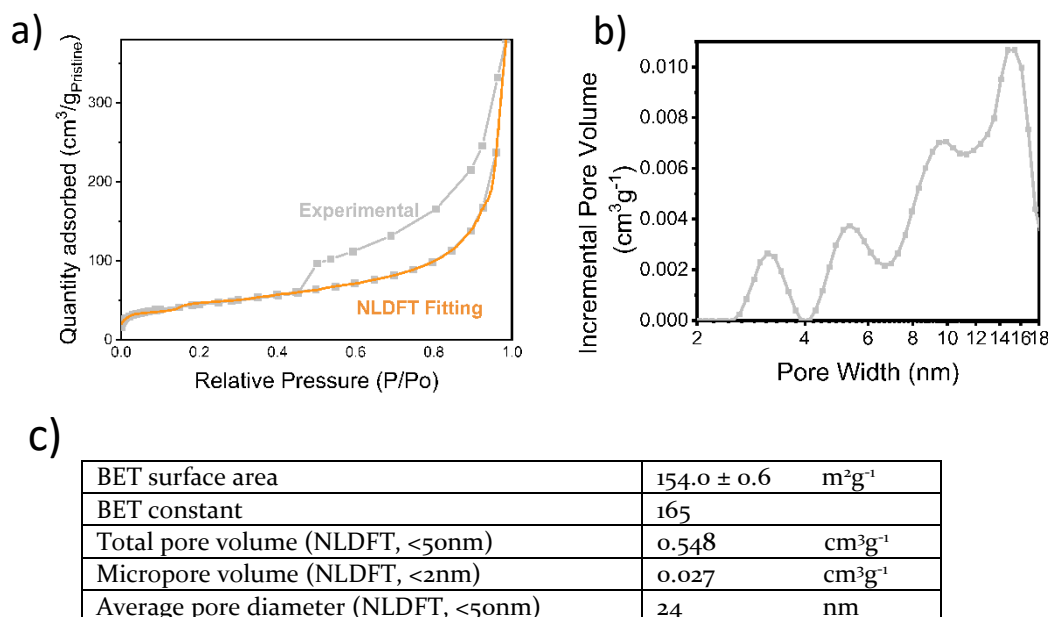


Figure S14. a) N₂ sorption isotherm of the pristine FePC/G catalyst. Comparison of the experimental data (grey) and the fitting (orange) with NLDFT for carbon slit pore

b) pore size distribution obtained from NLDFT for carbon slit pores, for the pristine FePC/G catalyst

c) Summary of porosity analysis results for the pristine catalyst

Inductively coupled plasma mass spectroscopy (ICP-MS)

ICP-MS was used to determine the iron content of the pristine FePC/G catalyst. This was determined to be 4.9 ± 0.1 %w, in line with the theoretical expected value of 4.91 %w

X-ray Photoelectron Spectroscopy (XPS)

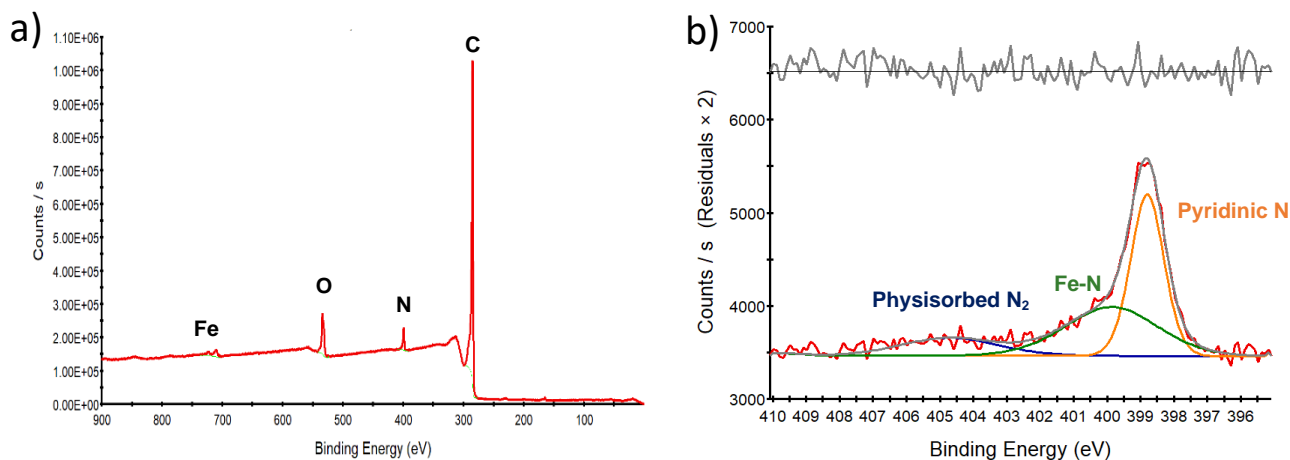


Figure S15: a) Results of XPS survey for the as-received FePC

b) Fitting of XPS N₂ results for the as-received FePC. The experimental data are shown in red, while the results of the fitting, and the fitting residuals are shown in gray. Three nitrogen species were used for the fitting: physisorbed N₂ (in blue), Fe-N (in green) and pyridinic nitrogen (in orange)

Table S2: results of the XPS survey on FePC

Name	Peak BE	FWHM eV	Area (P) CPS.eV	Atomic %
C1s	285.27	2.33	3132297	88.3
O1s	533.58	4.56	619309	7.23
N1s	399.23	2.33	206282.4	3.74
Fe2p	710.24	6.27	263869.5	0.72

Table S3: results of N2 XPS peak fitting on FePC

Name	Peak BE	FWHM eV	Area (P) CPS.eV	Atomic %
N1s - Physisorbed N2	404.70	3.37	705.52	14.9
N1s - Pyridinic N	398.80	1.16	2196.44	46.2
N1s - Fe-N	399.87	3.25	1850.94	38.9

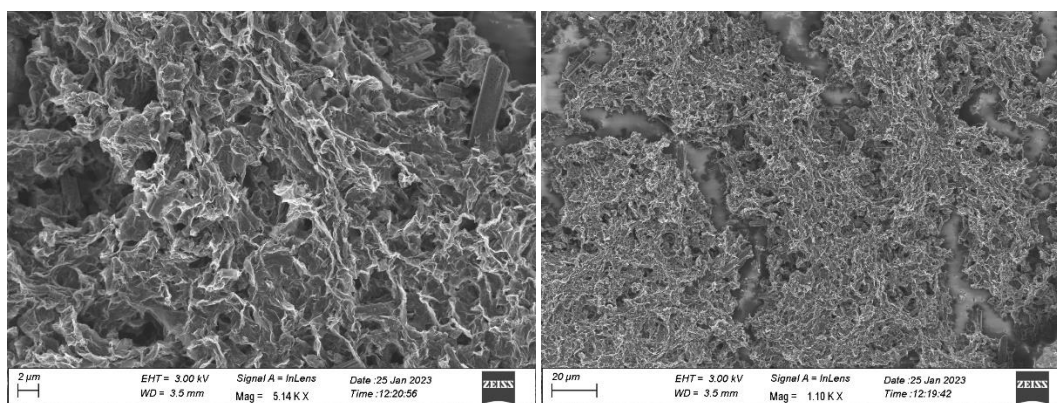


Figure S16: SEM images of the pristine catalyst drop-casted on a glass substrate. Scanning Electron Microscope (LEO Gemini 1252 FEG-SEM) operating at accelerating voltage of 3 keV and working distance around 3 mm. Before the measurement, the samples were secured onto the alumina sample holders using conductive double-sided carbon tapes. Conductive liquid silver paint was used to create effective conductivity path of the sample surface to prevent charge build-up.

S12. Bibliography

- Higgins, D., Zamani, P., Yu, A. & Chen, Z. The application of graphene and its composites in oxygen reduction electrocatalysis: a perspective and review of recent progress. *Energy Environ. Sci.* **9**, 357–390 (2016).
- Jiang, Y. *et al.* Enhanced Catalytic Performance of Pt-Free Iron Phthalocyanine by Graphene Support for Efficient Oxygen Reduction Reaction. *ACS Catal.* **3**, 1263–1271 (2013).
- Yu, T. *et al.* Preparation of FePcNs@GO composites and boosting oxygen reduction reaction. *Res. Chem. Intermed.* **48**, 3375–3387 (2022).
- Zhang, H. *et al.* Boosting the Performance of Iron-Phthalocyanine as Cathode Electrocatalyst for Alkaline Polymer Fuel Cells Through Edge-Closed Conjugation. *ACS Appl. Mater. & Interfaces* **10**, 28664–28671 (2018).
- Ngamchuea, K., Eloul, S., Tschulik, K. & Compton, R. G. Planar diffusion to macro disc electrodes—what electrode size is required for the Cottrell and Randles-Sevcik equations to apply quantitatively? *J. Solid State Electrochem.* **18**, 3251–3257 (2014).

6. Xiong, L. Amperometric Gas Sensing. 207 (2014).
7. Huango, X. J., Rogers, E. I., Hardacre, C. & Compton, R. G. The reduction of oxygen in various room temperature ionic liquids in the temperature range 293–318 K: Exploring the applicability of the Stokes–Einstein relationship in room temperature ionic liquids. *J. Phys. Chem. B* **113**, 8953–8959 (2009).
8. Evans, R. G., Klymenko, O. V., Saddoughi, S. A., Hardacre, C. & Compton, R. G. Electroreduction of oxygen in a series of room temperature ionic liquids composed of group 15-centered cations and anions. *J. Phys. Chem. B* **108**, 7878–7886 (2004).
9. Xiao, C., Rehman, A. & Zeng, X. Evaluation of the dynamic electrochemical stability of ionic liquid-metal interfaces against reactive oxygen species using an in situ electrochemical quartz crystal microbalance. *RSC Adv.* **5**, 31826–31836 (2015).
10. Nakamoto, H. *et al.* Ether-functionalized ionic liquid electrolytes for lithium-air batteries. *J. Power Sources* **243**, 19–23 (2013).
11. Vanhoutte, G., Hojniak, S. D., Bardé, F., Binnemans, K. & Fransaera, J. Fluorine-functionalized ionic liquids with high oxygen solubility. *RSC Adv.* **8**, 4525–4530 (2018).
12. Neale, A. R. *et al.* Effect of cation structure on the oxygen solubility and diffusivity in a range of bis(trifluoromethyl)sulfonylimide anion based ionic liquids for lithium-air battery electrolytes. *Phys. Chem. Chem. Phys.* **18**, 11251–11262 (2016).
13. Anthony, J. L., Anderson, J. L., Maginn, E. J. & Brennecke, J. F. Anion Effects on Gas Solubility in Ionic Liquids. *J. Phys. Chem. B* **109**, 6366–6374 (2005).
14. Song, T., Morales-Collazo, O. & Brennecke, J. F. Solubility and Diffusivity of Oxygen in Ionic Liquids. *J. Chem. Eng. Data* **64**, 4956–4967 (2019).
15. Monaco, S. *et al.* An electrochemical study of oxygen reduction in pyrrolidinium-based ionic liquids for lithium/oxygen batteries. *Electrochim. Acta* **83**, 94–104 (2012).
16. Bahadur, I., Osman, K., Coquelet, C., Naidoo, P. & Ramjugernath, D. Solubilities of carbon dioxide and oxygen in the ionic liquids methyl trioctyl ammonium bis(trifluoromethylsulfonyl)imide, 1-butyl-3-methyl imidazolium bis(trifluoromethylsulfonyl)imide, and 1-butyl-3-methyl imidazolium methyl sulfate. *J. Phys. Chem. B* **119**, 1503–1514 (2015).
17. Afzal, W., Liu, X. & Prausnitz, J. M. Solubilities of some gases in four imidazolium-based ionic liquids. *J. Chem. Thermodyn.* **63**, 88–94 (2013).
18. Kumelán, J., Kamps, Á. P. S., Urukova, I., Tuma, D. & Maurer, G. Solubility of oxygen in the ionic liquid [bmim][PF6]: Experimental and molecular simulation results. *J. Chem. Thermodyn.* **37**, 595–602 (2005).
19. Anthony, J. L., Maginn, E. J. & Brennecke, J. F. Solution thermodynamics of imidazolium-based ionic liquids and water. *J. Phys. Chem. B* **105**, 10942–10949 (2001).
20. Jacquemin, J., Costa Gomes, M. F., Husson, P. & Majer, V. Solubility of carbon dioxide, ethane, methane, oxygen, nitrogen, hydrogen, argon, and carbon monoxide in 1-butyl-3-methylimidazolium tetrafluoroborate between temperatures 283 K and 343 K and at pressures close to atmospheric. *J. Chem. Thermodyn.* **38**, 490–502 (2006).
21. Zhang, D., Okajima, T., Matsumoto, F. & Ohsaka, T. Electroreduction of Dioxygen in 1-n-Alkyl-3-methylimidazolium Tetrafluoroborate Room-Temperature Ionic Liquids. *J. Electrochem. Soc.* **151**, D31 (2004).
22. Husson-Borg, P., Majer, V. & Costa Gomes, M. F. Solubilities of oxygen and carbon dioxide in butyl methyl imidazolium tetrafluoroborate as a function of temperature and at pressures close to atmospheric pressure. *J. Chem. Eng. Data* **48**, 480–485 (2003).

23. Favero, S., Stephens, I. E. L. & Titirici, M. M. Engineering the Electrochemical Interface of Oxygen Reduction Electrocatalysts with Ionic Liquids: A Review. *Adv. Energy Sustain. Res.* **2**, 2000062 (2021).
24. Gaidukevič, J. *et al.* Synthesis of Reduced Graphene Oxide with Adjustable Microstructure Using Regioselective Reduction in the Melt of Boric Acid: Relationship Between Structural Properties and Electrochemical Performance. *Nanomaterials* vol. **8** (2018).
25. Tripathi, A. K., Verma, Y. L. & Singh, R. K. Thermal, electrical and structural studies on ionic liquid confined in ordered mesoporous MCM-41. *J. Mater. Chem. A* **3**, 23809–23820 (2015).
26. Heinze, M. T. *et al.* Solid-ionic liquid interfaces: Pore filling revisited. *Phys. Chem. Chem. Phys.* **16**, 24359–24372 (2014).
27. Sing, K. S. W. Reporting physisorption data for gas/solid systems with special reference to the determination of surface area and porosity. *Pure Appl. Chem.* **57**, 603–619 (1985).
28. Lapshin, D. N., Jorge, M., Campbell, E. E. B., Campbell, E. E. B. & Sarkisov, L. On competitive gas adsorption and absorption phenomena in thin films of ionic liquids. *J. Mater. Chem. A* **8**, 11781–11799 (2020).